

# 3D-Guided Scalable Flow Matching for Generating Volumetric Tissue Spatial Transcriptomics from Serial Histology

Mohammad Vali Sanian<sup>5,6,7,\*</sup> Arshia Hemmat<sup>4,7,\*</sup> Amirhossein Vahidi<sup>2,7,\*</sup>  
 Jonas Maaskola<sup>7</sup> Jimmy Tsz Hang Lee<sup>7</sup> Stanislaw Makarchuk<sup>7</sup>  
 Yeliz Demirci<sup>7</sup> Nana-Jane Chipampe<sup>7</sup> Muzlifah Haniffa<sup>2,3,7</sup>  
 Omer Bayraktar<sup>7,†</sup> Lassi Paavolainen<sup>6,†</sup> Mohammad Lotfollahi<sup>1,2,7,†</sup>

\*Equal contribution

† Correspondence Authors

<sup>1</sup>Cambridge Stem Cell Institute, University of Cambridge

<sup>2</sup>Cambridge Center for AI in Medicine, University of Cambridge

<sup>3</sup>Department of Medicine, University of Cambridge

<sup>4</sup>Computer Science Department, University of Oxford

<sup>5</sup>Computer Science Department, University of Helsinki

<sup>6</sup>Institute for Molecular Medicine Finland, University of Helsinki

<sup>7</sup>Wellcome Sanger Institute

## Abstract

A scalable and robust 3D tissue transcriptomics profile can enable a holistic understanding of tissue organization and provide deeper insights into human biology and disease. Most predictive algorithms that infer ST directly from histology treat each section independently and ignore 3D structure, while existing 3D-aware approaches are not generative and do not scale well. We present Holographic Tissue Expression Inpainting and Analysis (HoloTea), a 3D-aware flow-matching framework that imputes spot-level gene expression from H&E while explicitly using information from adjacent sections. Our key idea is to retrieve morphologically corresponding spots on neighboring slides in a shared feature space and fuse this cross section context into a lightweight ControlNet, allowing conditioning to follow anatomical continuity. To better capture the count nature of the data, we introduce a 3D-consistent prior for flow matching that combines a learned zero-inflated negative binomial (ZINB) prior with a spatial-empirical prior constructed from neighboring

sections. A global attention block introduces 3D H&E scaling linearly with the number of spots in the slide, enabling training and inference on large 3D ST datasets. Across three spatial transcriptomics datasets spanning different tissue types and resolutions, HoloTea consistently improves 3D expression accuracy and generalization compared to 2D and 3D baselines. We envision HoloTea advancing the creation of accurate 3D virtual tissues, ultimately accelerating biomarker discovery and deepening our understanding of disease.

## 1. Introduction

Spatial transcriptomics [40] links gene expression to tissue morphology and has transformed the way we study cellular states and disease-associated niches [15, 29] in situ [44]. Existing platforms (e.g., Visium, Xenium, CosMx) operate on 2D sections with a limited field of view, capturing only a thin slice of a much larger 3D tissue volume. This restricts our ability to probe vertical cell-cell communication, 3D tissue niches, and morphomolecular architectures that span multiple planes. Native 3D or thick-tissue in situ assays and 3D molecular atlases partially address this [7, 8, 37], but remain constrained by capture depth and area, long proto-

†Correspondence:

ob5@sanger.ac.uk

lassi.paavolainen@helsinki.fi

ml19@sanger.ac.uk

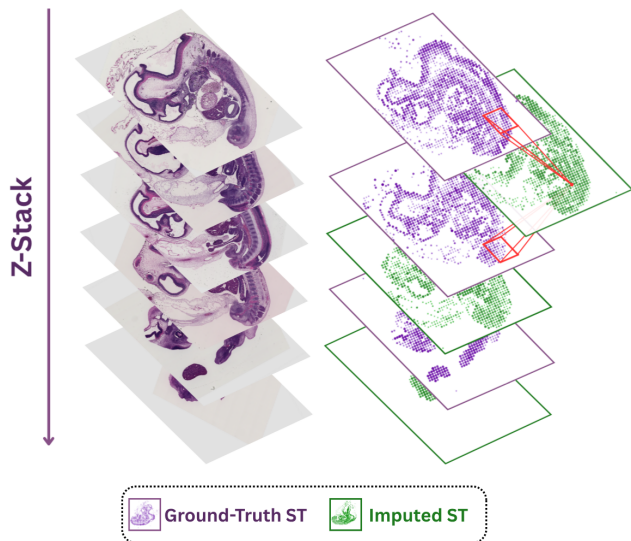


Figure 1. HoloTea leverages spatial neighborhood information from adjacent sections to improve 3D consistency in H&E to ST imputation.

cols, specialized instrumentation, and high cost. Another approach is to densely section the tissue and perform ST on many serial sections [32, 33], but this remains prohibitively expensive and labor-intensive to reconstruct full 3D volumes in routine studies.

In contrast, acquiring histology is cheap and scalable: tissues can be densely sectioned, H&E-stained, and imaged as serial whole-slide stacks, with ST performed only on a subset of sections. This naturally motivates computational models that leverage these dense histology stacks and sparse ST measurements to learn the 3D spatial structure of gene expression. By predicting 3D-consistent spatial transcriptomics from serial H&E, such models can reconstruct volumetric tissue molecular architecture without sequencing every section, enabling cost-effective, scalable analysis of 3D tissue niches and cell–cell communication in health and disease.

Within this emerging paradigm of H&E-based ST prediction, two main streams of work have appeared. The first focuses on whole-slide generative modeling with flow matching, exemplified by STFlow [12], which models the joint distribution of all spots on a slide using local spatial attention and efficient slide-level encoders. The second centers on probabilistic assignment and deconvolution frameworks such as ST-Assign [10], which integrate scRNA-seq references with ST to infer cell-type mixtures and domains. While effective, these approaches leave open two key gaps for 3D reconstruction from serial histology: (i) most H&E to ST predictors are trained per section and do not explicitly enforce 3D coherence across serial stacks, leading to drift along the  $z$ -axis; and (ii) the start distribution used by flow-matching

models is rarely tailored to the zero-inflated, overdispersed nature of gene counts [25, 26], placing undue burden on the denoiser early in the generative trajectory.

To address these gaps, we introduce HoloTea, a 3D H&E to ST leveraging flow matching [22, 24]. For each query spot on section  $z$ , we retrieve morphologically corresponding candidates on sections  $z\pm 1$  using  $(x, y)$  proximity and feature-space cosine similarity, then inject this adjacent context into selected denoiser blocks via a lightweight ControlNet [45]. This design promotes anatomical continuity across sections without heavy preprocessing. Because flow matching decouples the probability path from the start distribution, we can instantiate biology-compatible priors: a learned ZINB prior using the scVI parameterization [9, 25] and a 3D-consistent spatial–empirical prior constructed from neighboring sections. Compared to STFlow [12], we extend flow matching based ST generation from single 2D sections to the serial-section regime, coupling FM stability and slide-level efficiency with explicit 3D conditioning and biology-aligned priors for transcript count data. In contrast to ST-Assign [10], which relies on external scRNA-seq references and global mixture inference, our H&E-only generator is fully reference-free and incurs a training and inference cost that is linear in the number of spots (local kNN graphs plus  $O(Nm)$  inducing-point attention), naturally scaling to whole slides and serial stacks. An overview of the retrieval-conditioned flow-matching pipeline including  $z\pm 1$  neighbor search, adjacent-token aggregation, lightweight ControlNet conditioning, and ZINB-based priors is shown in Fig. 2.

### Our contributions are:

- An adjacent-slide conditioning scheme that retrieves morphologically matched context via cosine similarity and injects it with a spot-wise ControlNet.
- $z$ -aware, biology-compatible prior distributions for flow matching, including a learned ZINB prior and a spatial-empirical prior with light smoothing.
- A stable, scalable global attention to inject the global image features that scales linearly with the number of spots without scaling with the number of slides.
- We demonstrate the strong performance of our method across multiple datasets for whole slide gene expression generation task: HoloTea shows competitive results compared to other baselines.

## 2. Related Work

### 2.1. H&E to Expression prediction

Large-scale H&E to ST models have advanced along three axes: stronger multi-resolution encoders, better supervision/benchmarks, and generative objectives. TRIPLEX aggregates cellular-, meso-, and slide-scale cues with an explicit fusion module and shows consistent gains on Visium

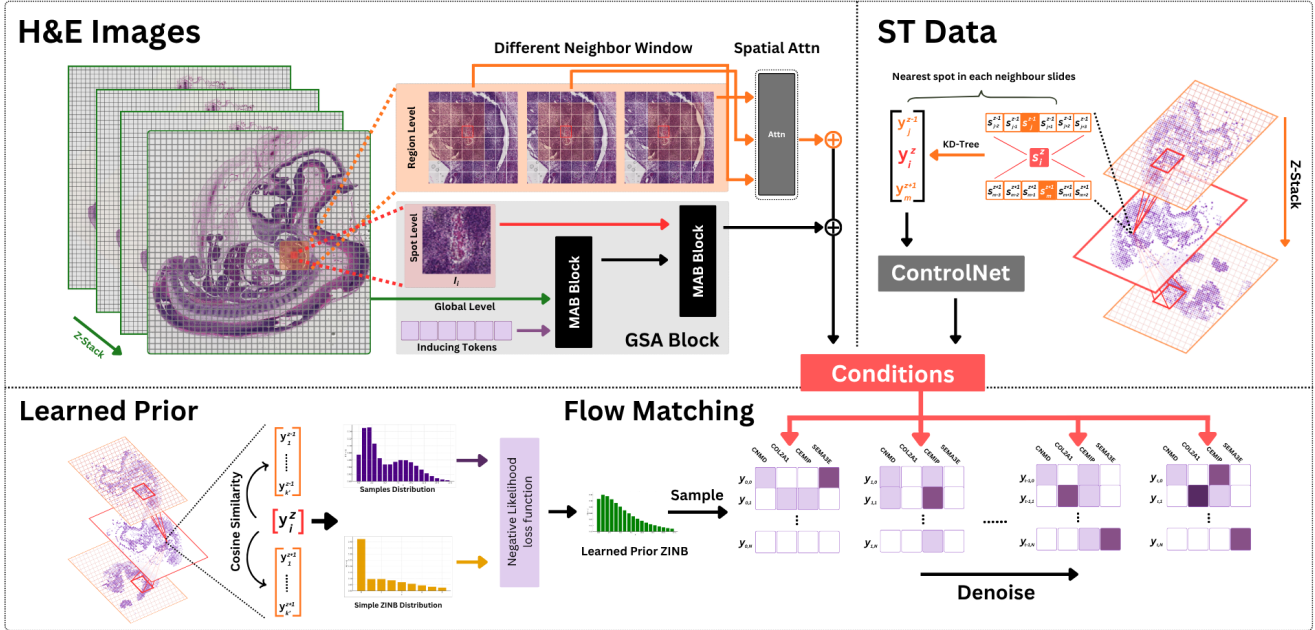


Figure 2. Method overview. For each query spot on section  $z$ , HoloTea retrieves nearest neighbors from sections  $z \pm 1$  using feature-space similarity, aggregates them into an adjacent token, and uses a ControlNet to condition the flow-matching denoiser with ZINB-based priors.

datasets [3]. SpaRED curates a 26-source benchmark with harmonized preprocessing and demonstrates that completing corrupted ST matrices significantly boosts downstream H&E to ST predictors [30]. Beyond purely discriminative regressors, recent generative approaches treat ST as a conditional generation problem: Stem leverages diffusion modeling to capture stochasticity in spot-level gene profiles given histology and reports SOTA across several datasets [48]. Complementary alignment-based methods (e.g., DANet) emphasize dynamic cross-modal alignment to couple image features with gene targets while accounting for gene–gene dependencies [42]. Meanwhile, multimodal contrastive formulations (e.g., mclSTExp) integrate spot context with transformer attention and image–omics contrastive learning [31]. Finally, pathology foundation encoders (UNI/UNI2) pretrained on 100M–200M patches are increasingly used as robust backbones for H&E feature extraction in ST pipelines [16, 20, 28].

## 2.2. 3D spatial transcriptomics and 3D imputation

On the data and systems side, Open-ST introduces practical end-to-end protocols and tooling for subcellular ST in 2D/3D, including serial-section registration and 3D “virtual tissue block” reconstruction that lower the barrier to volumetric studies [27, 34, 46]. For multi-slice analytics, SpaDo contributes cross-slice spatial domain detection, reference-

based annotation, and large-scale clustering across platforms, providing infrastructure to reason about consistency and heterogeneity in stacks [5]. In parallel, the field is moving toward larger multimodal corpora that pair WSIs with ST at scale: HEST-1k consolidates 1,229 paired ST and H&E samples (2.1M expression–morphology pairs) and a library that standardizes ingestion and benchmarking, facilitating 3D/stack-aware evaluation and the use of strong pathology backbones for volumetric imputation [13, 14, 19].

## 3. Preliminary

### 3.1. Problem setup

We consider serial sections indexed by  $z \in \{1, \dots, Z\}$  with spot sets  $\mathcal{S}_z$ , where each spot  $i \in \mathcal{S}_z$  has planar coordinates and section index  $\mathbf{s}_i = (a_i, b_i, z_i)$ . For each spot we have an H&E tile  $I_i$ , a target gene-expression vector  $\mathbf{y}_i \in \mathbb{R}_{\geq 0}^G$  (raw counts or  $\log(1+\cdot)$ ), and an image embedding  $\mathbf{v}_i = \phi(I_i) \in \mathbb{R}^D$  from a pretrained encoder  $\phi(\cdot)$ . Our goal is to impute  $\hat{\mathbf{y}}_i$  from  $(I_i, \mathbf{s}_i)$  with high within-section fidelity and across- $z$  coherence. Within each section we build a  $k$ -nearest-neighbor ( $k$ -NN) graph in  $(a, b)$ , and the section index  $z$  is used subsequently for prior construction and cross-section conditioning.

### 3.2. Background

**Flow matching.** We model imputation as transport from a start distribution  $p_0$  over gene vectors to the data distribution  $p_1$  via a time-dependent field learned with flow matching (FM). For each spot  $i$ , we draw a start sample  $\mathbf{x}_{0,i} \sim p_0$  and define a linear (displacement) path to the target  $\mathbf{x}_{1,i} \equiv \mathbf{y}_i$ ,

$$\mathbf{x}_{t,i} = (1-t)\mathbf{x}_{0,i} + t\mathbf{x}_{1,i}, \quad t \in [0, 1], \quad (1)$$

where  $t$  is the scalar time along the path. A time-conditioned network  $f_\theta$  (parameters  $\theta$ ) predicts the clean endpoint from partial information,

$$\hat{\mathbf{y}}_i = f_\theta(\mathbf{x}_{t,i}, \mathbf{c}_i, t), \quad \mathbf{c}_i = [\mathbf{v}_i, \mathbf{s}_i, \text{kNN}(i)], \quad (2)$$

where  $\mathbf{c}_i$  concatenates the image features  $\mathbf{v}_i$ , the coordinates  $\mathbf{s}_i$ , and a neighborhood summary  $\text{kNN}(i)$  (the indices or pooled features of the  $k$  nearest spots to  $i$  within its section). We minimize the supervised endpoint-regression loss  $\mathcal{L}_{\text{fm}} = \mathbb{E}_{i,t} [\|\hat{\mathbf{y}}_i - \mathbf{y}_i\|_2^2]$ , following standard FM practice for displacement or straight paths [6, 22, 23].

**Zero-Inflated Negative Binomial (ZINB).** A practical strength of FM is that the objective above does not depend on the form of  $p_0$ , so we can choose a starting prior that matches the domain to shorten the transport. *STFlow* adopts a ZINB prior for gene counts due to over-dispersion and excess zeros in ST data [12]. Following the scVI [9, 25], for each gene  $g$  and spot  $i$  we use mean  $\mu_{i,g} > 0$ , inverse-dispersion  $\theta_g > 0$ , and zero-inflation probability  $\pi_{i,g} \in (0, 1)$ , with Negative Binomial pmf

$$\text{NB}(y | \mu, \theta) = \frac{\Gamma(y + \theta)}{\Gamma(\theta) y!} \left( \frac{\theta}{\theta + \mu} \right)^\theta \left( \frac{\mu}{\theta + \mu} \right)^y, \quad y \in \mathbb{N}, \quad (3)$$

and ZINB mixture

$$p(y | \mu, \theta, \pi) = \pi \mathbb{1}\{y = 0\} + (1 - \pi) \text{NB}(y | \mu, \theta). \quad (4)$$

Here  $y$  is the gene-count random variable,  $\Gamma(\cdot)$  is the gamma function, and the ZINB parameters may include library-size factors in  $\mu_{i,g}$  and logit parameterization for  $\pi_{i,g}$  as in scVI. We sample  $\mathbf{Y}_i \sim \prod_{g=1}^G \text{ZINB}(\mu_{i,g}, \theta_g, \pi_{i,g})$  and map to the model domain via  $\mathbf{x}_{0,i} = \log(1 + \mathbf{Y}_i)$ . ZINB is standard for scRNA-seq and ST likelihoods [35] and is implemented in scVI-TOOLS [9].

**STFlow denoiser.** The denoiser  $f_\theta$  operates on a within-section  $k$ -NN graph  $G = (V, E)$  to perform spatial denoising conditioned on histology. Each node  $i$  forms a token by concatenating the current state  $\mathbf{x}_{t,i}$ , a time embedding  $e(t)$ , positional features derived from  $\mathbf{s}_i$ , and its image embedding  $\mathbf{v}_i$ . Multi-head attention aggregates neighboring evidence

with edge-aware biases  $b_{ij}$  (functions of spatial relations such as  $\|\mathbf{s}_i - \mathbf{s}_j\|$ ), using

$$\alpha_{ij} = \text{softmax}_j \left( \frac{\mathbf{q}_i^\top \mathbf{k}_j}{\sqrt{d}} + b_{ij} \right), \quad \mathbf{h}_i = \sum_{j \in \mathcal{N}(i)} \alpha_{ij} \mathbf{v}_j^{(\text{val})}, \quad (5)$$

where  $\mathbf{q}_i, \mathbf{k}_j, \mathbf{v}_j^{(\text{val})}$  are the query, key, and value vectors for spots  $i$  and  $j$ ,  $d$  is the per-head key/query dimensionality,  $\mathcal{N}(i)$  is the  $k$ -NN set of  $i$ ,  $\alpha_{ij}$  are attention weights, and  $\mathbf{h}_i$  is the aggregated representation. This graph-attention view follows established formulations [39] and can be equipped with inducing-point self-attention for low-rank global mixing [21]; see also the whole-slide, locally attentive denoiser in STFlow [12].

## 4. Method

Our method contains three main components: (i) conditioning from adjacent spots on the closest slides together with a prior over gene-gene relations in training dataset; (ii) applying conditioning and  $z$ -variation through ControlNet [45]; and (iii) building hierarchical feature selection efficiently via Global set attention (GSA) [21].

### 4.1. Adjacent-section conditioning

For a query spot  $i \in \mathcal{S}_z$ , we form a candidate set from adjacent sections

$$\mathcal{A}(i) = \text{kNN}_{k'}((x_i, y_i); \mathcal{S}_{z-1} \cup \mathcal{S}_{z+1}), \quad (6)$$

where  $(x_i, y_i)$  are the planar coordinates of spot  $i$ ,  $\mathcal{S}_{z\pm 1}$  are the spot sets on the adjacent sections  $z\pm 1$  in the training data, and  $k'$  is the candidate-pool size returned by the  $k$ -NN query in  $(x, y)$ . We then compute feature-space cosine similarities

$$s_{ij} = \frac{\langle \mathbf{v}_i, \mathbf{v}_j \rangle}{\|\mathbf{v}_i\| \|\mathbf{v}_j\|}, \quad j \in \mathcal{A}(i), \quad (7)$$

where  $\mathbf{v}_i, \mathbf{v}_j \in \mathbb{R}^D$  are image embeddings from a pretrained encoder for the query and candidate spots. Weights use a temperature  $\tau > 0$  and a spatial blend coefficient  $\beta \in [0, 1]$ :

$$w_{ij} = \text{softmax}((1 - \beta) s_{ij}^{\text{cos}} + \beta s_{ij}^{\text{xy}} / \tau), \quad (8)$$

where  $s_{ij}^{\text{cos}}$  is the cosine score above,  $s_{ij}^{\text{xy}}$  is a spatial affinity (e.g., a decreasing function of  $\|(x_i, y_i) - (x_j, y_j)\|$ ), and the softmax is taken over  $j \in \mathcal{A}(i)$  to yield  $\sum_j w_{ij} = 1$ . At training, when  $\mathbf{y}_j \in \mathbb{R}_{\geq 0}^G$  is available on  $z\pm 1$ , we build the adjacent token

$$\tilde{\mathbf{g}}_i^{\text{adj}} = \sum_{j \in \mathcal{A}(i)} w_{ij} \mathbf{P} \mathbf{y}_j, \quad (9)$$

with  $\mathbf{P} \in \mathbb{R}^{r \times G}$  a low-rank projection (e.g., selecting top-variance genes or a learned  $r$ -dimensional gene subspace).

At inference, we substitute the *current flow state* from adjacent sections,

$$\tilde{\mathbf{g}}_i^{\text{adj}} = \sum_{j \in \mathcal{A}(i)} w_{ij} \mathbf{P} \mathbf{x}_{t,j}, \quad (10)$$

where  $\mathbf{x}_{t,j}$  is the interpolant state at time  $t$  for spot  $j$  (Sec. 3.2), keeping the pipeline H&E-only at test time.

**ControlNet injection.** A lightweight CNN (ControlNet) processes a coarse gene map built from  $\mathbf{x}_t$  (GeneMapBuilder; grid size  $H \times W$  and channel count  $C$  define the spatial resolution and feature depth of the map). We sample per-spot control tokens via `grid.sample` at the continuous coordinates  $(x_i, y_i)$  to obtain

$$\mathbf{u}_i = h_\omega(\tilde{\mathbf{g}}_i^{\text{adj}}, t) \in \mathbb{R}^{d_u}, \quad (11)$$

where  $h_\omega(\cdot)$  is a small MLP/CNN conditioned on time  $t$ , and  $d_u$  is the control-token dimensionality. These tokens are injected into selected transformer blocks as a residual modulation,

$$\text{block}_\ell \leftarrow \text{block}_\ell + \alpha_\ell(t) \text{Proj}_\ell(\mathbf{u}_i), \quad (12)$$

where  $\text{Proj}_\ell(\cdot)$  linearly matches  $\mathbf{u}_i$  to the block’s hidden size, and  $\alpha_\ell(t)$  is a warm-up schedule in  $t$  to avoid early oversteering; a sharp variant is used to preserve high-frequency detail. This follows the conditioning principle of ControlNet [45] while adapting it to spot-wise conditioning.

## 4.2. $z$ -aware priors

**Learned ZINB prior.** We *pretrain* a predictor  $\psi_\eta$  to map spot features to per-spot ZINB parameters,

$$\psi_\eta : (\mathbf{v}_i, \mathbf{s}_i) \mapsto (\boldsymbol{\mu}_i, \boldsymbol{\theta}_i, \boldsymbol{\pi}_i) \in \mathbb{R}_{>0}^G \times \mathbb{R}_{>0}^G \times (0, 1)^G, \quad (13)$$

where  $\boldsymbol{\mu}_i$  are per-gene means,  $\boldsymbol{\theta}_i$  inverse-dispersions, and  $\boldsymbol{\pi}_i$  zero-inflation probabilities (scVI parameterization [9, 25]; see ZINB in Sec. 3.2). The pretraining minimizes the negative log-likelihood of the ZINB model on the training expressions:

$$\mathcal{L}_{\text{ZINB}}(\eta) = - \sum_{i \in \mathcal{D}_{\text{train}}} \sum_{g=1}^G \log p_{\text{ZINB}}(y_{i,g} | \mu_{i,g}, \theta_{i,g}, \pi_{i,g}), \quad (14)$$

with  $(\mu_{i,g}, \theta_{i,g}, \pi_{i,g})$  given by  $\psi_\eta(\mathbf{v}_i, \mathbf{s}_i)$ . After convergence we *freeze*  $\psi_\eta$  and use it solely to define the flow start: sample counts

$$\mathbf{Y}_i \sim \prod_{g=1}^G \text{ZINB}(\mu_{i,g}, \theta_{i,g}, \pi_{i,g}), \quad \mathbf{x}_{0,i} = \log(1 + \mathbf{Y}_i). \quad (15)$$

No gradients from the flow-matching loss backpropagate into  $\psi_\eta$ ; the start distribution  $p_0$  is therefore fixed during FM training.

## 4.3. Global set attention (GSA)

To inject global context without quadratic cost in the number of spots  $N$ , we use a two-stage attention block inspired by the Induced Set Attention Block (ISAB) [21]. Let  $\mathbf{X} \in \mathbb{R}^{N \times d}$  be spot tokens (per spot: current state  $\mathbf{x}_{t,i}$ , H&E features, time/positional embeddings) and let  $\mathbf{S} \in \mathbb{R}^{m \times d}$  be a small set of inducing tokens ( $m \ll N$ ), learned and shared across batches. We use multi-head attention  $\text{MHA}(\mathbf{Q}, \mathbf{K}, \mathbf{V}) = \text{Concat}_h(\text{softmax}(\mathbf{Q}\mathbf{K}^\top / \sqrt{d_h})\mathbf{V})\mathbf{W}^\mathcal{O}$  with  $h$  heads and per-head width  $d_h = d/h$ .

Stage 1 (global read): the inducing tokens query all spots to form a global summary

$$\mathbf{H} = \text{MHA}(\mathbf{S}, \mathbf{X}, \mathbf{X}) \in \mathbb{R}^{m \times d}, \quad (16)$$

which aggregates whole-slide information into  $m$  slots. Stage 2 (global write): each spot then attends to this compact summary

$$\mathbf{Y} = \text{MHA}(\mathbf{X}, \mathbf{H}, \mathbf{H}) \in \mathbb{R}^{N \times d}, \quad (17)$$

injecting global context back into all spots. We apply pre-norm residual blocks around both stages (LayerNorm  $\rightarrow$  MHA  $\rightarrow$  Dropout  $\rightarrow$  Residual) followed by a position-wise MLP with residual. The computational cost scales as  $O(Nmd)$  rather than  $O(N^2d)$ , so global information is propagated across an entire slide without attention cost growing with the number of spots. In practice we pick  $m$  (e.g.,  $m=32-128$ ) to trade fidelity for memory;  $m$  can be held fixed across datasets, making GSA a drop-in global context module for whole-slide and 3D stacks.

## 4.4. Inference

We impute expression without ground-truth  $\mathbf{y}$  by marching the flow from  $t=0$  to  $t=1$  while reusing adjacent-section context. Let  $\{t_s\}_{s=0}^S$  be a monotone grid with  $t_0=0$ ,  $t_S=1$  and step sizes  $\eta_s = t_{s+1} - t_s$ . (1) Initialization: compute (or load)  $\mathbf{v}_i = \phi(I_i)$ ; sample a start  $\mathbf{x}_{0,i}$  per spot from the chosen prior (learned\_zinb: use  $\psi_\eta$  to get  $(\boldsymbol{\mu}_i, \boldsymbol{\theta}_i, \boldsymbol{\pi}_i)$  and sample ZINB; spatial\_empirical: draw from cross-section neighbors). (2) Time stepping: for  $s=0, \dots, S-1$ , set  $\mathbf{x}_{t_s,i} = (1-t_s)\mathbf{x}_{0,i} + t_s \mathbf{x}_{1,i}$  with the unknown endpoint replaced by the model’s current estimate; build adjacent candidates  $\mathcal{A}(i)$  on  $z \pm 1$  and compute weights  $w_{ij}$  from cosine/spatial scores; form  $\tilde{\mathbf{g}}_i^{\text{adj}} = \sum_{j \in \mathcal{A}(i)} w_{ij} \mathbf{P} \mathbf{x}_{t_s,j}$  (note the use of *current flow states* from adjacent sections); derive ControlNet tokens  $\mathbf{u}_i$  and run the Spatial Transformer with GSA to obtain  $\hat{\mathbf{y}}_i^{(s)}$ . (3) State update: advance along the straight path toward the prediction,

$$\mathbf{x}_{t_{s+1},i} \leftarrow (1 - \eta_s) \mathbf{x}_{t_s,i} + \eta_s \hat{\mathbf{y}}_i^{(s)}. \quad (18)$$

Table 1. Performance across the HER2, ST-Data, and in-house embryo datasets on highly variable gene sets.

Model	HER2				ST-Data (images)				In-house embryo			
	MSE ( $\downarrow$ )	MAE ( $\downarrow$ )	PCC ( $\uparrow$ )		MSE ( $\downarrow$ )	MAE ( $\downarrow$ )	PCC ( $\uparrow$ )		MSE ( $\downarrow$ )	MAE ( $\downarrow$ )	PCC ( $\uparrow$ )	
			SPOT	GENE			SPOT	GENE			SPOT	GENE
UNI	1.093	0.859	0.509 $\pm$ 0.094	0.259 $\pm$ 0.231	0.769	0.699	0.569 $\pm$ 0.077	0.332 $\pm$ 0.149	0.261	0.296	0.506 $\pm$ 0.224	0.613 $\pm$ 0.203
STFlow	0.477	0.534	0.740 $\pm$ 0.125	0.620 $\pm$ 0.146	0.443	0.532	0.775 $\pm$ 0.080	0.540 $\pm$ 0.142	0.255	0.270	0.557 $\pm$ 0.248	0.663 $\pm$ 0.166
ASIGN 3D	0.462	0.563	0.704 $\pm$ 0.113	0.607 $\pm$ 0.112	0.481	0.551	0.741 $\pm$ 0.013	0.531 $\pm$ 0.121	0.701	0.791	0.311 $\pm$ 0.208	0.412 $\pm$ 0.080
<b>Our Method</b>	<b>0.455</b>	<b>0.523</b>	<b>0.744 <math>\pm</math> 0.114</b>	<b>0.638 <math>\pm</math> 0.145</b>	<b>0.364</b>	<b>0.468</b>	<b>0.796 <math>\pm</math> 0.073</b>	<b>0.612 <math>\pm</math> 0.132</b>	<b>0.199</b>	<b>0.235</b>	<b>0.576 <math>\pm</math> 0.245</b>	<b>0.691 <math>\pm</math> 0.173</b>

---

### Algorithm 1 HoloTea training algorithm

---

**Require:** Dataset  $\{(I_i, \mathbf{y}_i, \mathbf{s}_i)\}$ ; encoder  $\phi$ ; projection  $\mathbf{P}$ ; kNN sizes  $k, k'$ ; blend  $\beta$ , temperature  $\tau$ ; ControlNet scales  $\{\alpha_\ell(t)\}$ ; inducing count  $m$ ; time sampler  $t \sim \mathcal{T}$ ; optimizer (AdamW); early-stopping on validation.

**Ensure:** Trained denoiser  $\theta$ , ControlNet  $\omega$ ; frozen ZINB prior  $\psi_\eta$ .

**Phase A: Pretrain ZINB prior (frozen later)**

- 1: **for epoch** = 1, . . . ,  $E_{\text{ZINB}}$  **do**
  - 2:   **for minibatch**  $\mathcal{B}$  **do**
  - 3:     Compute H&E embeddings  $\mathbf{v}_i \leftarrow \phi(I_i)$  for  $i \in \mathcal{B}$ .
  - 4:     Predict ZINB parameters  $(\boldsymbol{\mu}_i, \boldsymbol{\theta}_i, \boldsymbol{\pi}_i) = \psi_\eta(\mathbf{v}_i, \mathbf{s}_i)$ .
  - 5:     Accumulate ZINB NLL using Eq. (14); update  $\eta$ .
  - 6:     Early-stop on validation NLL if applicable.
  - 7:   Freeze  $\psi_\eta$  (no gradients in Phase B).
  - 8:   **Phase B: Flow-matching training**
  - 9:    **for step** = 1, . . . ,  $T$  **do**
  - 10:     Sample a minibatch  $\mathcal{B}$  of spots (possibly across sections); sample  $t \sim \mathcal{T}$ .
  - 11:     **Start sampling:** for each  $i \in \mathcal{B}$ , sample counts via Eq. (15) using frozen  $\psi_\eta$ , then map to model space with Eq. (3.2).
  - 12:     **Interpolant:** compute  $\mathbf{x}_{t,i}$  using Eq. (1).
  - 13:     **Adjacent conditioning (train):** build  $\mathcal{A}(i)$  by Eq. (6); scores  $s_{ij}^{\text{cos}}$  and spatial affinities  $s_{ij}^{\text{xy}}$ ; weights  $w_{ij}$  by Eq. (8); adjacent token  $\tilde{\mathbf{g}}_i^{\text{adj}}$  by Eq. (9).
  - 14:     **ControlNet:** compute  $\mathbf{u}_i$  by Eq. (11); inject into selected blocks via Eq. (12).
  - 15:     **Backbone with GSA:** run the spatial transformer, applying GSA read and write per Eqs. (16)–(17).
  - 16:     **Prediction & loss:** obtain  $\hat{\mathbf{y}}_i$ ; backpropagate the FM loss Eq. (3.2); update  $\theta, \omega$  (and any unfrozen heads).
  - 17:     Apply gradient clipping, mixed precision, and early-stopping on validation sections as needed.
  - 18:   **Return**  $\theta, \omega$  (trained),  $\psi_\eta$  (frozen).
- 

## 5. Experiments

### 5.1. Experiments settings

**Datasets.** We evaluate on two public benchmarks: the **HER2** multi-section breast cancer dataset [1] and the **ST-Data** breast cancer cohort introduced with ST-Net [11]. We follow the authors’ preprocessing and adopt section-level holdouts for testing (entire heldout sections), mirroring typical cross-section protocols described for these datasets. Moreover, we benchmark on the **in-house Embryo dataset** (to be released soon in a separate manuscript), it contains a 3D stack of serial embryo sections profiled with 10X Vi-

sium HD, yielding dense spot-level transcript counts co-registered with H&E whole-slide images (and optional auxiliary imaging channels). The stack provides a multi-modal volume (H&E + ST) across 52 slides of z-stack of H&E.

**Implementation details.** All experiments use PyTorch with mixed precision, Adam optimizer [17], and a single NVIDIA H100 (80 GB). H&E tiles are encoded by the UNI pathology foundation model [2]. Our ZINB decoder follows the scVI parameterization and NLL [9, 25], taking as input either the STFlow latent representation or features from the frozen UNI pathology encoder [2]. In the UNI baseline, we keep the UNI backbone fixed and train only this ZINB head, yielding an image-only encoder–decoder model without any flow-based components. Flow training uses displacement/rectified flow matching [22, 23], and our ControlNet-style conditioning for  $z$ -aware guidance follows [45]. The training follows Algorithm 1.

For ASIGN 3D [47], we re-ran the method on the HER2 and ST imputation tasks using the normalization described in [12], enabling a fair comparison of MAE and MSE. On the in-house embryo dataset, the original ASIGN 3D configuration resulted in out-of-memory (OOM) errors even with a batch size of one; therefore, we reduced the model size by removing one graph neural network layer, and all reported results for this dataset correspond to that reduced configuration. Hyperparameters are listed in Appendix S2.

**Gene sets.** We report results on two panels: (i) **Top-250 HVG** selected with Scanpy’s `pp.highly_variable_genes` (Seurat-flavor) [36, 41]; (ii) **Custom gene set**, built by detecting spatially variable genes (SVGs) per section via SPARK-X [38], intersecting the top- $K$  SVGs within sliding windows of five consecutive sections, and taking the union across windows to stabilize across- $z$  morphology; (iii) **marker genes** for 106 anatomical regions were identified by performing differential gene expression analysis. Selecting the top two marker genes for each region yielded a set of 211 distinct genes.

**Evaluation metrics.** We compute spot-wise Pearson correlation coefficient (PCC spot), gene-wise Pearson correlation coefficient (PCC gene) and MSE on held-out sections.

## 5.2. Gene Expression Imputation

We perform 3D spatial imputation as generating a whole slide gene expression from serial H&E sections, given ground-truth ST on only a subset of sections. We adopt two complementary splits. (i) Following the ASIGN 3D-ST imputation task [47], each 3D sample provides a single ST-labeled section used for supervision, while all remaining sections in the same stack are ST-unlabeled and serve as imputation targets. Then models are trained across samples and evaluated on entire held-out sections without using their ST during training. (ii) Even-slice hold-out. Within each 3D stack, we hold out every even-index section ( $z=2, 4, \dots$ ) as test targets and train on the odd-index sections ( $z=1, 3, \dots$ ), using only their ST labels. This split probes across- $z$  generalization under a fixed anatomy and avoids reliance on any single ‘known’ slice.

We conduct both splits on two public multi-section breast datasets, HER2 [1] and ST-Data [11]. For our in-house embryo dataset, we use the even-slice hold-out split to simulate missing-through-plane acquisition at scale. We report the results for the whole-slide imputation task in Tab. S1 and Tab. 2. HoloTea outperforms other methods across all three datasets and splits. ASIGN performs poorly on Embryo since the memory scales with number of slides and number of spots per slide, we discuss the details in Sec. 5.4.

Table 2. Performance across in-house embryo datasets using custom gene panels.

Model	MSE ( $\downarrow$ )	MAE ( $\downarrow$ )	PCC ( $\uparrow$ )	
			Spot	Gene
UNI	0.412	0.398	0.554 $\pm$ 0.249	0.663 $\pm$ 0.111
STFlow	0.387	0.381	0.581 $\pm$ 0.103	0.700 $\pm$ 0.104
ASIGN 3D	0.76	0.8	0.314 $\pm$ 0.213	0.401 $\pm$ 0.112
Ours	<b>0.330</b>	<b>0.343</b>	<b>0.598 <math>\pm</math> 0.105</b>	<b>0.726 <math>\pm</math> 0.105</b>

## 5.3. HoloTea captures expression morphology of anatomical marker genes

We trained a model for the 211 marker genes on the in-house embryo dataset, see Sec. S3. Tab. 3 visualizes the expression patterns for some marker genes of two different anatomical regions, the basal plate (CNMD and COL2A1) and the cardinal vein (CEMIP and SEMA3E), showing ground truth and imputed expression across 3 of the 26 sections held out during training. It is notable that the imputed expression patterns closely recapitulate the ground truth expression, while reducing expression variance in the low-count regime. In particular, for the basal plate markers, the imputed expression patterns exhibit segmentation along the spinal cord, and imputed expression in the anatomical region of the cardinal vein is observed for its marker genes. Further, while secondary regions with lower expression are also recapitulated in the imputed data, binary shot noise is suppressed.

Jointly clustering the ground truth and imputed expression of all 26 unseen sections (Tab. 3, Sec. S3, and Figs. S1 to S3) shows that imputed expression clusters recapitulate those of the ground truth, with a normalized mutual information of 0.524. The ground truth clusters have a lower neighbor consistency of  $0.775 \pm 0.109$  than the imputed clusters,  $0.880 \pm 0.045$ , indicating that the imputed clusters are more spatially contiguous.

Overall, these results suggest that imputing expression on interleaved sections is feasible. Additional details about experimental results can be found in Sec. S3.

## 5.4. Computational Complexity

We design our method to scale with the axial depth  $z$  (number of sections). As the number of slides and therefore the number of spots  $N$  increases, ASIGN encounters GPU out-of-memory (OOM) on our in-house dataset (see Tab. 4). In contrast, the compute and memory footprint of our method grows approximately linearly in  $z$  during training. At inference time, we only require features from the adjacent sections ( $z \pm 1$ ) for each target section, which substantially reduces GPU demand. In Tab. 4 we report both FLOPs and GPU memory for our method during training, and for single-slide inference (one slide at test time). For clarity, FLOPs are measured per sample, and training memory is reported at peak usage. Notably, the original ASIGN implementation from the authors’ codebase yields OOM on a single H100 GPU (80 GB) on our dataset.

This favorable scaling is a direct consequence of the design. First, adjacent retrieval limits cross-section interactions to a small candidate pool from  $z \pm 1$ , so each spot computes only  $O(k')$  cosine similarities; with encoder features cached, this overhead is negligible relative to attention. Second, the ControlNet that injects cross-section cues is a shallow CNN/MLP whose cost is linear in the number of spots. Third, the backbone replaces quadratic global attention with local  $k$ NN attention and an optional low-rank inducing-attention module that scales as  $O(Nm)$  (with  $m \ll N$ ) instead of  $O(N^2)$ . Together, these choices keep both FLOPs and memory near-linear in  $z$  during training and reduce the inference footprint (adjacent sections only), explaining the robustness to OOM we observe compared with ASIGN.

Table 4. Computational complexity on in-house embryo dataset: number of spots ( $N$ ), forward-pass FLOPs, and peak GPU memory.

Model	# Spots ( $N$ )	GFLOPs	Memory [GB]
ASIGN (3D)	327 532	-	OOM
Our method (Train)	327 532	333.21	26.9
Our method (Inference)	327 532	114.9	3.7

Table 3. True and imputed spatial expression patterns of marker genes for the basal plate (CNMD and COL2A1) and for the cardinal vein (CEMIP and SEMA3E) across multiple sections unseen during training. Last pair of columns: results of a joint clustering of all 26 sections. GT: ground truth, Imp: imputed. Color scale for gene expression: low  high. Best viewed at high magnification.

Section	CNMD		COL2A1		CEMIP		SEMA3E		Cluster	
	GT	Imp	GT	Imp	GT	Imp	GT	Imp	GT	IMP
22										
54										
124										

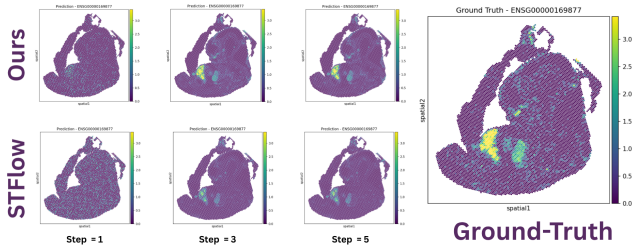


Figure 3. Comparison of spatial gene-expression predictions for AHSP: our method (top), STFlow (bottom), and ground truth (right) across different flow steps.

## 6. Ablation

To quantify the contribution of each architectural component, we compare four variants of our model on the in-house embryo dataset and evaluate them on the even-slice hold-out. We sweep over marker panel sizes of 50, 100, 200, and 500 genes, and report spot-level mean squared error (MSE), mean absolute error (MAE), and Pearson correlation coefficient (PCC) in Table S10. The four regimes are: (i) Vanilla STFlow, our base model; (ii) Vanilla + Learned Prior, which augments STFlow with a learned ZINB prior; (iii) ControlNet + Learned Prior, which additionally uses ControlNet-style conditioning; and (iv) ControlNet + Cross-Cosine + Learned Prior, which further adds our cross-slide cosine branch.

**Effect of the learned prior.** Introducing the learned ZINB prior has a mixed but generally positive effect relative to Vanilla STFlow. For the 100 and 200 gene panels it lowers both MSE and MAE while slightly improving PCC (e.g., at 200 genes MSE drops from 0.176 to 0.161 and PCC increases from 0.673 to 0.680). At 50 and 500 genes the prior alone does not consistently outperform the baseline,

suggesting that prior learning is most helpful for medium-sized panels where the gene space is neither too sparse nor overly wide.

**Effect of ControlNet conditioning.** Adding ControlNet on top of the learned prior yields consistent gains over both Vanilla STFlow and the prior only model. For the 50 gene panel, PCC increases from 0.693 (vanilla) and 0.691 (prior only) to 0.701, while MSE decreases to 0.154, the best among all regimes at this panel size. Similar trends hold at 100 and 200 genes, where ControlNet improves PCC to roughly 0.69-0.70 with reduced MSE/MAE. Even for the widest 500 gene panel, ControlNet remains beneficial. Qualitative comparison of predicted spatial expression patterns for gene AHSP, for our ControlNet-based model (top row) and STFlow (bottom row) across flow steps (1, 3, 5), with ground-truth expression shown on the right Fig. 3. Our model, which is equipped with ControlNet and cross-slide conditioning, more faithfully recovers the high-expression clusters and fine-grained structures than STFlow, visually reinforcing the quantitative gains reported in the ablation study (Table S10).

**Effect of the cross-slide cosine branch.** Our full model, which augments ControlNet with the cross-slide cosine branch, delivers the strongest overall performance. At 100 and 200 genes it achieves the best scores across all three metrics (e.g., at 200 genes MSE improves from 0.155 to 0.147 and PCC from 0.694 to 0.698). At 500 genes, where all methods degrade slightly due to the larger panel, the cross-slide branch still improves over the prior-only variant (MAE 0.128 vs. 0.134; PCC 0.654 vs. 0.642) and attains the highest PCC among all regimes. These results indicate that cross-slide cues provide complementary long-range context beyond what ControlNet and the learned prior capture on

Table 5. Spot-level performance on the even-slice hold-out split for different ablation settings on the in-house embryo dataset. For each panel size, the best value is shown in **bold**. Lower is better for MSE/MAE; higher is better for PCC. Due to space constraints, the *Learned Prior* row is omitted; the full table is provided in the Supplementary Material S3.

Regime	Genes	MSE ↓	MAE ↓	PCC(GENE) ↑
Vanilla STFlow	50	0.160	0.107	0.693
	100	0.177	0.120	0.688
	200	0.176	0.119	0.673
	500	0.164	<b>0.124</b>	0.646
ControlNet + Learned Prior	50	<b>0.154</b>	0.096	<b>0.701</b>
	100	0.169	0.117	0.692
	200	0.155	0.108	0.694
	500	0.164	0.127	0.651
ControlNet + Learned Prior + Cross Slide Neighbors	50	0.155	<b>0.092</b>	0.695
	100	<b>0.158</b>	<b>0.112</b>	<b>0.697</b>
	200	<b>0.147</b>	<b>0.108</b>	<b>0.698</b>
	500	<b>0.162</b>	0.128	<b>0.654</b>

their own.

## 7. Conclusion

We presented HoloTea, a 3D-aware H&E to ST generative model that couples flow-matching with (i) **3D context** by retrieving morphologically corresponding spots from adjacent sections and ControlNet-based injection of those cues, (ii) **Generalization** with biology-compatible priors over gene counts, and (iii) **Scalability**: we introduce a scalable transformer backbone with low-rank global context. Across public breast datasets and a large in-house embryo stack, HoloTea delivers stronger spot and gene-wise correlations and reduced reconstruction error than prior H&E to ST methods, with ablations confirming complementary gains from the learned prior, ControlNet conditioning, and the cross-slide branch. The architecture also scales favorably with stack depth: training and inference remain near-linear in the number of sections, avoiding the memory blow-ups that affect some 3D baselines.

## References

- [1] Alma Andersson, Ludvig Larsson, Linnea Stenbeck, Fredrik Salmén, Anna Ehinger, Sunny Z Wu, Ghamdan Al-Eryani, Daniel Roden, Alex Swarbrick, Åke Borg, et al. Spatial deconvolution of HER2-positive breast cancer delineates tumor-associated cell type interactions. *Nature Communications*, 12 (6012), 2021. 6, 7
- [2] Richard J. Chen, Tong Ding, Ming Y. Lu, Drew F. K. Williamson, Guillaume Jaume, et al. Towards a general-purpose foundation model for computational pathology. *Nature Medicine*, 2024. 6
- [3] Youngmin Chung, Ji Hun Ha, Kyeong Chan Im, and Joo Sang Lee. Accurate spatial gene expression prediction by integrating multi-resolution features. In *Proceedings of the IEEE/CVF Conference on Computer Vision and Pattern Recognition (CVPR)*, 2024. 3
- [4] Ozan Ciga, Tony Xu, and Anne Louise Martel. Self supervised contrastive learning for digital histopathology. *Machine Learning with Applications*, 7:100198, 2022. 2
- [5] Bin Duan, Shaoqi Chen, Xiaojie Cheng, and Qi Liu. Multi-slice spatial transcriptome domain analysis with spado. *Genome Biology*, 25(73), 2024. 3
- [6] Patrick Esser, Sumith Kulal, Andreas Blattmann, Rahim Entezari, Jonas Müller, Harry Saini, Yam Levi, Dominik Lorenz, Axel Sauer, Frederic Boesel, Dustin Podell, Tim Dockhorn, Zion English, Kyle Lacey, Alex Goodwin, Yannik Marek, and Robin Rombach. Scaling rectified flow transformers for high-resolution image synthesis. *arXiv preprint arXiv:2403.03206*, 2024. 4
- [7] Rongxin Fang, Aaron R Halpern, Mohammed Mostafizur Rahman, Zhengkai Huang, Zhiyun Lei, Sebastian J Hell, Catherine Dulac, and Xiaowei Zhuang. Three-dimensional single-cell transcriptome imaging of thick tissues. 2024. 1
- [8] Valentina Gandin, Jun Kim, Liang-Zhong Yang, Yumin Lian, Takashi Kawase, Amy Hu, Konrad Rokicki, Greg Fleishman, Paul Tillberg, Alejandro Aguilera Castrejon, Carsen Stringer, Stephan Preibisch, and Zhe J. Liu. Deep-tissue transcriptomics and subcellular imaging at high spatial resolution. *Science*, 388(6744):eadq2084, 2025. 1
- [9] Adam Gayoso, Romain Lopez, Galen Xing, Pierre Boyeau, Valeh Valiollah Pour Amiri, Justin Hong, Katherine Wu, Michael Jayasuriya, Edouard Mehlman, Maxime Langevin, Yining Liu, Jules Samaran, Gabriel Misrachi, Achille Nazaret, Oscar Clivio, Chenling Xu, Tal Ashuach, Mariano Gabitto, Mohammad Lotfollahi, Valentine Svensson, Eduardo da Veiga Beltrame, Vitalii Kleshchevnikov, Carlos Talavera-López, Lior Pachter, Fabian J. Theis, Aaron Streets, and Nir Yosef. A python library for probabilistic analysis of single-cell omics data. *Nature Biotechnology*, 40(2):163–166, 2022. 2, 4, 5, 6
- [10] Krzysztof Gorgoń et al. St-assign: a probabilistic model for joint cell-type annotation in scrna-seq and mixture decomposition in spatial transcriptomics. *bioRxiv*, 2023. 2
- [11] Bryan He, Ludvig Bergenstråhle, Linnea Stenbeck, Abubakar Abid, Alma Andersson, Åke Borg, Jonas Maaskola, Joakim Lundeberg, and James Zou. Integrating spatial gene expres-

- sion and breast tumour morphology via deep learning. *Nature Biomedical Engineering*, 4(8):827–834, 2020. 6, 7
- [12] Tinglin Huang, Tianyu Liu, Mehrtash Babadi, Wengong Jin, and Rex Ying. Scalable generation of spatial transcriptomics from histology images via whole-slide flow matching. *arXiv preprint arXiv:2506.05361*, 2025. ICML 2025 Spotlight (project page: <https://graph-and-geometric-learning.github.io/projects/stflow>). 2, 4, 6
- [13] Guillaume Jaume and colleagues. Hest-1k: Neurips 2024 poster/project page, 2024. 3
- [14] Guillaume Jaume, Paul Doucet, Andrew H. Song, et al. Hest-1k: A dataset for spatial transcriptomics and histology image analysis. In *NeurIPS Datasets & Benchmarks*, 2024. 3
- [15] Kazumasa Kanemaru, James Cranley, Daniele Muraro, Antonio M. A. Miranda, Siew Yen Ho, Anna Wilbrey-Clark, Jan Patrick Pett, Krzysztof Polanski, Laura Richardson, Monika Litvinukova, Natsuhiko Kumasaka, Yue Qin, Zuzanna Jablonska, Claudia I. Semprich, Lukas Mach, Monika Dabrowska, Nathan Richoz, Liam Bolt, Lira Mamanova, Rakesh Lal Kapuge, Sam N. Barnett, Shani Perera, Carlos Talavera-López, Iliaria Mulas, Krishnaa T. Mahubani, Liz Tuck, Lu Wang, Margaret M. Huang, Martin Prete, Sophie Pritchard, John Dark, Kourosh Saeb-Parsy, Minal Patel, Menna R. Clatworthy, Norbert Hübner, Rasheda A. Chowdhury, Michela Nosedà, and Sarah A. Teichmann. Spatially resolved multiomics of human cardiac niches. *Nature*, 619(7971):801–810, 2023. 1
- [16] Jakob N. Kather, Eike Wulczyn, et al. Towards a general-purpose foundation model for computational pathology. *Nature Medicine*, 2024. 3
- [17] Diederik P. Kingma and Jimmy Ba. Adam: A method for stochastic optimization. In *International Conference on Learning Representations (ICLR)*, 2015. 6
- [18] Dominik Klein, Giovanni Palla, Marius Lange, Michal Klein, Zoe Piran, Manuel Gander, Laetitia Meng-Papaxanthos, Michael Sterr, Lama Saber, Changying Jing, Aimée Bastidas-Ponce, Perla Cota, Marta Tarquis-Medina, Shrey Parikh, Ilan Gold, Heiko Lickert, Mostafa Bakhti, Mor Nitzan, Marco Cuturi, and Fabian J. Theis. Mapping cells through time and space with moscot. *Nature*, 638(8052):1065–1075, 2025. 1
- [19] Mahmood Lab. Hest-library: Integrating histology and spatial transcriptomics, 2024. 3
- [20] Mahmood Lab. Uni: Pathology foundation model (code repository), 2024. 3
- [21] Juho Lee, Yoonho Lee, Jungtaek Kim, Adam R. Kosiorek, Seungjin Choi, and Yee Whye Teh. Set transformer: A framework for attention-based permutation-invariant neural networks. In *Proceedings of the 36th International Conference on Machine Learning*, pages 3744–3753. PMLR, 2019. 4, 5
- [22] Yaron Lipman, Ricky T. Q. Chen, Heli Ben-Hamu, Maximilian Nickel, and Matthew Le. Flow matching for generative modeling. In *ICLR*, 2023. 2, 4, 6
- [23] Xingchao Liu, Chengyue Gong, and Qiang Liu. Flow straight and fast: Learning to generate and transfer data with rectified flow. *arXiv:2209.03003*, 2022. 4, 6
- [24] Xingchao Liu, Chengyue Gong, and Qiang Liu. Flow straight and fast: Learning to generate and transfer data with rectified flow. In *International Conference on Learning Representations (ICLR)*, 2023. 2
- [25] Romain Lopez, Jeffrey Regier, Michael B. Cole, Michael I. Jordan, and Nir Yosef. Deep generative modeling for single-cell transcriptomics. *Nature Methods*, 15(12):1053–1058, 2018. 2, 4, 5, 6
- [26] Romain Lopez, Baoguo Li, Hadas Keren-Shaul, Pierre Boyeau, Merav Kedmi, David Pilzer, Adam Jelinski, Ido Yofe, Eyal David, Allon Wagner, Can Ergen, Yoseph Addadi, Ofra Golani, Franca Ronchese, Michael I. Jordan, Ido Amit, and Nir Yosef. Destvi identifies continuums of cell types in spatial transcriptomics data. *Nature Biotechnology*, 40(9):1360–1369, 2022. 2
- [27] Andrea Luo, Malte Kühnemund, et al. Protocol for high-resolution 3d spatial transcriptomics using open-st. *STAR Protocols*, 2025. 3
- [28] MahmoodLab. Uni: Pathology foundation model (model card), 2025. 3
- [29] Colleen McGregor, Xiao Qin, Marta Jagielowicz, Tarun Gupta, Zinan Yin, Verena Lentsch, David Fawcner-Corbett, Vy Wien Lai, Paula Gomez Castro, Esther Bridges, Chloe Hyun-Jung Lee, Huei-Wen Chuang, Lei Deng, Anna Aulicino, Renuka Teague, Sorayya Moradi, Jun Sung Park, Jeongmin Woo, Kexin Xu, Ruchi Tandon, Nicole Cianci, Jan Bornschein, Ling-Pei Ho, Paulina Siejka-Zielinska, Zoe Christoforidou, Sarah Hill, Johannes Lehmann, Rhea Kujawa, Paola Vargas Gutierrez, Carol Cheng, Maria Greco, Katherine Baker, Mark Bignell, Bruce George, Eve Fryer, Michael Vieth, Agne Antanaviciute, and Alison Simmons. Spatial fibroblast niches define crohn’s fistulae. *Nature*, 2025. 1
- [30] Gabriel Mejia, Daniela Ruiz, Paula Cárdenas, Leonardo Manrique, Daniela Vega, and Pablo Arbeláez. Spared benchmark: Enhancing gene expression prediction from histology images with spatial transcriptomics completion. *arXiv preprint arXiv:2407.13027*, 2024. 3
- [31] Wenwen Min, Zhiceng Shi, Jun Zhang, Jun Wan, and Changmiao Wang. Multimodal contrastive learning for spatial gene expression prediction using histology images. *Briefings in Bioinformatics*, 25(6):bbae551, 2024. 3
- [32] Chia-Kuei Mo, Jingxian Liu, Siqi Chen, Erik Storrs, Andre Luiz N. Targino da Costa, Andrew Houston, Michael C. Wendl, Reyka G. Jayasinghe, Michael D. Iglesia, Cong Ma, John M. Herndon, Austin N. Southard-Smith, Xinhao Liu, Jacqueline Mudd, Alla Karpova, Andrew Shinkle, S. Peter Goedegebuure, Abdurrahman Taha Mousa Ali Abdelzاهر, Peng Bo, Lauren Fulghum, Samantha Livingston, Metin Balaban, Angela Hill, Joseph E. Ippolito, Vesteinn Thorsson, Jason M. Held, Ian S. Hagemann, Eric H. Kim, Peter O. Bayguinov, Albert H. Kim, Mary M. Mullen, Koresh I. Shoghi, Tao Ju, Melissa A. Reimers, Cody Weimholt, Liang-I Kang, Sidharth V. Puram, Deborah J. Veis, Russell Pachynski, Katherine C. Fuh, Milan G. Chheda, William E. Gillanders, Ryan C. Fields, Benjamin J. Raphael, Feng Chen, and Li Ding. Tumour evolution and microenvironment interactions in 2d and 3d space. *Nature*, 634(8036):1178–1186, 2024. 2
- [33] Michelli Faria de Oliveira, Juan Pablo Romero, Meii Chung, Stephen R. Williams, Andrew D. Gottscho, Anushka Gupta, Susan E. Pilipauskas, Seayar Mohabbat, Nandhini Raman, David J. Sukovich, David M. Patterson, Michelli Faria de Oliveira, Sarah E. B. Taylor, and Visium HD Development

- Team. High-definition spatial transcriptomic profiling of immune cell populations in colorectal cancer. *Nature Genetics*, 57(6):1512–1523, 2025. 2
- [34] Rajewsky Lab. 3d reconstruction from serial sections of spatial transcriptomics and h&e images (open-st documentation), 2024. 3
- [35] Davide Risso, Fanny Perraudeau, Svetlana Gribkova, Sandrine Dudoit, and Jean-Philippe Vert. A general and flexible method for signal extraction from single-cell rna-seq data. *Nature Communications*, 9:284, 2018. 4
- [36] Tim Stuart, Andrew Butler, Paul Hoffman, and et al. Comprehensive integration of single-cell data. *Cell*, 177(7):1888–1902.e21, 2019. 6
- [37] Xin Sui, Jennifer A Lo, Shuchen Luo, Yichun He, Zefang Tang, Zuwan Lin, Yiming Zhou, Wendy Xueyi Wang, Jia Liu, and Xiao Wang. Scalable spatial single-cell transcriptomics and translomics in 3D thick tissue blocks. 2024. 1
- [38] Shiquan Sun, Jiaqiang Zhu, and Xiang Zhou. Spark-x: non-parametric modeling enables scalable and robust detection of spatially expressed genes for spatial transcriptomic studies. *Genome Biology*, 22(351), 2021. 6
- [39] Petar Velickovic, Guillem Cucurull, Arantxa Casanova, Adriana Romero, Pietro Liò, and Yoshua Bengio. Graph attention networks. In *International Conference on Learning Representations (ICLR)*, 2018. 4
- [40] Cameron G. Williams, Hyun Jae Lee, Takahiro Asatsuma, Roser Vento-Tormo, and Ashraful Haque. An introduction to spatial transcriptomics for biomedical research. *Genome Medicine*, 14(1):68, 2022. 1
- [41] F. Alexander Wolf, Philipp Angerer, and Fabian J. Theis. Scanpy: large-scale single-cell gene expression data analysis. *Genome Biology*, 19(1):15, 2018. 6
- [42] Yulong Wu, Jin Xie, Jing Nie, Jiale Cao, Yuansong Zeng, and Zheng Wang. Danet: spatial gene expression prediction from h&e histology images through dynamic alignment. *Briefings in Bioinformatics*, 26(4), 2025. 3
- [43] Hanwen Xu, Naoto Usuyama, Jaspreet Bagga, Sheng Zhang, Rajesh Rao, Tristan Naumann, Cliff Wong, Zelalem Gero, Javier González, Yu Gu, Yanbo Xu, Mu-Hsin Wei, Wenhui Wang, Shuming Ma, Furu Wei, Jianwei Yang, Chunyuan Li, Jianfeng Gao, Jaylen Rosemon, Tucker Bower, Soohee Lee, Roshanthi Weerasinghe, Bill J. Wright, Ari Robicsek, Brian Piening, Carlo Bifulco, Sheng Wang, and Hoifung Poon. A whole-slide foundation model for digital pathology from real-world data. *Nature*, 630(8015):181–188, 2024. 2
- [44] Linlin Zhang, Dongsheng Chen, Dongli Song, Xiaoxia Liu, Yanan Zhang, Xun Xu, and Xiangdong Wang. Clinical and translational values of spatial transcriptomics. *Signal Transduction and Targeted Therapy*, 7(1):111, 2022. 1
- [45] Lvmin Zhang, Anyi Rao, and Maneesh Agrawala. Adding conditional control to text-to-image diffusion models. In *ICCV*, 2023. 2, 4, 5, 6
- [46] X. Zhang and colleagues. Open-st is an end-to-end experimental and computational workflow for subcellular spatial transcriptomics in 2d or 3d at low cost. *Cell*, 2024. 3
- [47] Junchao Zhu, Ruining Deng, Tianyuan Yao, Juming Xiong, Chongyu Qu, Junlin Guo, Siqi Lu, Mengmeng Yin, Yu Wang, Shilin Zhao, Haichun Yang, and Yuankai Huo. Assign: An anatomy-aware spatial imputation graphic network for 3d spatial transcriptomics. In *Proceedings of the IEEE/CVF Conference on Computer Vision and Pattern Recognition (CVPR)*, pages 30829–30838, 2025. 6, 7, 2
- [48] Sichen Zhu, Yuchen Zhu, Molei Tao, and Peng Qiu. Diffusion generative modeling for spatially resolved gene expression inference from histology images. In *International Conference on Learning Representations (ICLR), Poster*, 2025. See also arXiv:2501.15598. 3

# 3D-Guided Scalable Flow Matching for Generating Volumetric Tissue Spatial Transcriptomics from Serial Histology

## Supplementary Material

### S1. Dataset Details

#### S1.1. In-house embryo dataset.

To generate the in-house Embryo Spatial Transcriptomics (ST) dataset, we performed *10x Genomics Visium Cytassist* experiments on 62 serial sagittal sections obtained from a single Formalin-Fixed Paraffin-Embedded (FFPE) tissue block of a whole human embryo at Carnegie Stage 17 and after quality control, we retained 52 slides for our benchmark. Each section encompassed the full anatomical landscape of the embryo, covering major organ systems and developing structures. The FFPE block was sectioned at a thickness of  $5\ \mu\text{m}$  using a *Leica RM2235* microtome. Each Cytassist capture area contained an array of barcoded spots for spatially resolved mRNA capture and gene expression profiling.

The spatial transcriptomic data were processed using the *Space Ranger v2.10* pipeline with standard quality control procedures. In total, the dataset comprises 327,532 spatial spots, with a median of 7,618 spots under tissue. The average median number of genes detected per spot across all sections is approximately 7,173, providing high spatial resolution across the developing embryo.

#### S1.2. Public datasets.

**HER2 dataset.** For the HER2 cohort we used the spatial transcriptome sequencing data from eight HER2 positive human breast tumors, where each tumor contributes three or six spatial transcriptomics sections, giving a total of 36 profiled sections. These samples were generated with the first generation Spatial Transcriptomics in situ capturing arrays and sequenced on an Illumina NextSeq 550 platform, yielding whole transcriptome counts for each capture spot. The original study combines these data with single cell RNA sequencing from additional HER2 positive tumors to deconvolve each spot into proportions of major cell types, including epithelial, myeloid, T, B, plasma, endothelial and cancer associated fibroblast populations, and reports that a typical spot aggregates roughly 0 to 200 cells. A pathologist manually annotated one section per tumor into regions such as in situ cancer, invasive cancer, immune infiltrate, adipose tissue and connective tissue, and expression based clustering plus pathway enrichment were then used to define cancer and immune core signatures and to map tertiary lymphoid like structures and type I interferon related immune niches across all 36 sections.

**ST-data (Integrating spatial gene expression and breast tumour morphology via deep learning).** The ST-data cohort originates from the work of He et al., who introduced ST Net using a spatial transcriptomics dataset that links histopathology to local gene expression in breast cancer. The public release contains triplicate spatial transcriptomics sections from 23 patients spanning luminal A, luminal B, HER2-positive, and triple negative subtypes, for a total of 68 sections and 30,612 spatial locations with matched hematoxylin and eosin whole slide images. Each capture spot has a diameter of about 100 micrometer on the original in situ capturing array, and the corresponding histology was digitized at 20x, so that a 224 by 224 pixel image patch centered on each spot covers roughly 150 by 150 micrometer of tissue. The sequencing depth in the original study results in a median of around 3,400 counts and several thousand detected genes per spot, and ST Net was trained to predict the log expression of a curated panel of 250 target genes from these image patches using a leave one patient out cross validation protocol. This dataset therefore, provides a well-curated benchmark with consistent pre-processing, subtype labels, and tumor or normal tissue annotations, which we reuse as a standard testbed for evaluating our method on two-dimensional sections.

#### S1.3. Spatial alignment of Visium slides

**Data alignment.** For the **public** datasets (*HER2* and *ST-data*), we obtained the raw data from the original studies' official repositories and did *not* perform any additional alignment beyond the preprocessing carried out by the original authors. In contrast, for our **in-house embryo** dataset, we applied the two-stage alignment workflow described below.

**Stage 1: Pre-alignment with MOSCOT.** We first pre-aligned a total of 52 individual Visium slides non-consecutive but ordered according to their sectioning sequence using *MOSCOT*[18]. *MOSCOT* leverages spatial transcriptomics to align sets of two dimensional Visium spots into a coherent pseudo three dimensional volume. All sections were registered to a single reference slide selected from the middle of the stack, and the corresponding transformation matrices produced by *MOSCOT* were extracted. These matrices were then applied to pre-align the full-resolution H&E images, which we downscaled by a factor of two, resulting in a final pixel size of approximately  $0.45\ \mu\text{m}$ .

Table S1. Performance across the HER2, ST-Data, and in-house embryo datasets on highly variable gene sets.

Model	HER2				ST-Data (images)				In-house embryo			
	MSE ( $\downarrow$ )	MAE ( $\downarrow$ )	PCC ( $\uparrow$ )		MSE ( $\downarrow$ )	MAE ( $\downarrow$ )	PCC ( $\uparrow$ )		MSE ( $\downarrow$ )	MAE ( $\downarrow$ )	PCC ( $\uparrow$ )	
			SPOT	GENE			SPOT	GENE			SPOT	GENE
UNI	1.093	0.859	0.509 $\pm$ 0.094	0.259 $\pm$ 0.231	0.769	0.699	0.569 $\pm$ 0.077	0.332 $\pm$ 0.149	0.261	0.296	0.506 $\pm$ 0.224	0.613 $\pm$ 0.203
CIGA	0.865	0.738	0.494 $\pm$ 0.135	0.465 $\pm$ 0.143	0.7825	0.706	0.541 $\pm$ 0.083	0.247 $\pm$ 0.137	0.449	0.438	0.399 $\pm$ 0.194	0.427 $\pm$ 0.229
Gigapath	0.611	0.615	0.581 $\pm$ 0.126	0.576 $\pm$ 0.161	0.674	0.649	0.597 $\pm$ 0.076	0.364 $\pm$ 0.145	0.314	0.322	0.457 $\pm$ 0.223	0.554 $\pm$ 0.225
STFlow	0.477	0.534	0.740 $\pm$ 0.125	0.620 $\pm$ 0.146	0.443	0.532	0.775 $\pm$ 0.080	0.540 $\pm$ 0.142	0.255	0.270	0.557 $\pm$ 0.248	0.663 $\pm$ 0.166
ASIGN 3D	0.462	0.563	0.704 $\pm$ 0.113	0.607 $\pm$ 0.112	0.481	0.551	0.741 $\pm$ 0.013	0.531 $\pm$ 0.121	0.701	0.791	0.311 $\pm$ 0.208	0.412 $\pm$ 0.080
<b>Our Method</b>	<b>0.455</b>	<b>0.523</b>	<b>0.744 <math>\pm</math> 0.114</b>	<b>0.638 <math>\pm</math> 0.145</b>	<b>0.364</b>	<b>0.468</b>	<b>0.796 <math>\pm</math> 0.073</b>	<b>0.612 <math>\pm</math> 0.132</b>	<b>0.199</b>	<b>0.235</b>	<b>0.576 <math>\pm</math> 0.245</b>	<b>0.691 <math>\pm</math> 0.173</b>

**Stage 2: Fine registration with *pystackreg*.** The pre-aligned image stack served as input for fine-grained image registration implemented with the Python package *pystackreg*. We used the green (G) channel of the H&E images providing the highest contrast for alignment. Affine registration (translation, rotation, scaling, shear) was performed sequentially: each section was registered to its immediate predecessor (e.g., section 2 to section 1, section 3 to section 2, and so on). This produced a finely registered image stack and an updated set of transformation matrices.

**Final spot-coordinate update.** To obtain Visium spot coordinates corresponding to the fully registered images, we applied the transformation matrices from the fine-registration step to the MOSCOT-aligned spot positions, yielding the final coordinates used in downstream analyses. The implementation will be released following peer review.

### S1.4. Gene panel definitions.

For completeness, we summarize the three gene panels used throughout the main paper.

- **HVG panel.** A highly variable gene (HVG) panel obtained per dataset using a standard Scanpy pipeline (library-size normalization,  $\log(1+x)$  transform, and variance ranking). In the main paper we report results for the HVG-250 configuration.
- **Custom panel.** A dataset-specific panel constructed by combining spatially variable genes and genes of prior biological interest (for example, pathway genes and marker sets suggested in the original dataset releases).
- **Marker panel.** A curated set of 211 marker genes associated with 106 anatomical regions in the embryo stack. This panel is used for the clustering and neighbor-consistency analysis described in the main paper.

These panels correspond to the sets referred to as (i) HVG, (ii) custom, and (iii) marker genes in the main text.

## S2. Experiments Details

**Spot-centric visual features.** For each spatial spot, we extract a  $224 \times 224$  image patch centered at the spot from the whole-slide image, pass it through a frozen pre-trained foundation encoder, and use the resulting global embedding as the node feature for that spot.

The key hyperparameters used to train the model are summarized in the table S2.

**Dataset splits.** For all public datasets, we follow the official train/test partitions used in the ASIGN paper [47] to ensure fair comparisons. Unless otherwise noted, all metrics are reported on the held-out sections.

**Baseline training protocol.** For all baselines built on pathology foundation encoders (UNI, CIGA, and GigaPath) we follow a consistent training protocol that mirrors HoloTea as closely as possible. The pathology encoder weights are kept frozen, and we train only the downstream ZINB decoder and, where applicable, the flow-matching components, using the optimization hyperparameters listed in Table S3. This ensures that differences in performance primarily reflect the choice of encoder and our 3D-aware architecture rather than differences in training budget. For the ASIGN (3D) baseline we adapt the official configuration to our preprocessing and normalization pipeline and train until validation performance plateaus or GPU memory is exhausted on the largest embryo stack.

**Alternative pathology encoders.** In addition to the UNI pathology backbone in the main experiments, we also study the effect of swapping the image encoder while keeping the rest of the pipeline fixed. Specifically, in the appendix we repeat our experiments with two frozen H&E encoders: (i) the self-supervised contrastive histopathology model of Ciga et al. [4], pretrained on large collections of unlabeled whole-slide images; and (ii) the GigaPath whole-slide foundation model for digital pathology [43]. For both variants, we extract patch features with the pretrained encoder, freeze all its weights, and train only the ZINB decoder (and, where applicable, the flow-matching components) using the same optimizer, learning rate schedule, and training budget as in the UNI setup. This yields image-only encoder-decoder baselines that isolate the impact of the pathology backbone on 3D imputation performance.

**Global context tokens  $m$ .** All experiments use the global context mechanism described in the main paper, parameterized by the number of inducing tokens  $m$ . For each dataset we perform a small sweep from

$$m \in \{0, 4, 8, 16, 32, 64, 128, 256\}$$

Table S2. Core model hyperparameters (defaults).

Parameter	Default
Backbone layers $L$	4
Hidden dimension $d$	128
Pairwise / edge dimension	128
Attention heads	4
$k$ nearest neighbors	8
Dropout / Attention dropout	0.2 / 0.2
Global context (inducing tokens $m$ )	based on hyperparameter search

on a held-out split (see Tables S6–S8), and then select  $m$  per dataset based on performance and the trade-off between accuracy and compute. In practice, moderate values of  $m$  already capture most of the benefit, while very large values provide only marginal additional gains at a higher computational cost.

Table S3. Training and inference hyperparameters.

Parameter	Default / Setting
Batch size (slide-level)	2
Epochs	100
Optimizer / Learning rate	Adam / $5 \times 10^{-4}$
Gradient clipping (L2)	1.0
Time conditioning	Sinusoidal $\rightarrow$ MLP
Inference steps ( $S$ )	5

### S3. Results Details

**Complexity and dataset scale.** The embryo dataset used in our experiments consists of 327,532 spatial spots across the 3D stack (see Table S9). The complexity numbers reported in Table 4 of the main paper are measured per slide within this stack and should be interpreted in the context of this overall scale: the global attention backbone with  $m$  inducing tokens enables training and inference to scale approximately linearly with the number of spots per slide and with the depth of the stack.

**Randomness and variability.** Unless otherwise stated, all metrics in the main paper are reported for a single trained model per configuration. For each metric we aggregate over all spots or all genes in the corresponding test set, which substantially reduces statistical noise. Additional runs with different random seeds on a subset of configurations showed only minor fluctuations in the reported metrics, so we omit per-seed averages for brevity and focus on the main configuration in the tables.

Table S4. Priors and optional modules.

Component	Default / Setting
Prior sampler	ZINB (default)
ZINB parameters	total_count = 1, logits = 0.1, zi_logits = 0.0
Learned ZINB prior ( $\phi_e$ )	optional (frozen at train time)
Spatial-empirical prior	optional ( $k=128$ neighbors across $z \pm 1$ )
ControlNet conditioning	optional; channels = 32, grid = 64, scale = 1.0

Table S5. Foundation encoders and node-feature dimensions. Encoders are frozen.

Encoder	Patch size	Output dim
UNI v1 (official)	224×224	1024
GigaPath	224×224	1536
CIGA	224×224	512

**Clustering** Clustering of true and predicted counts was performed using routines implemented in the `scanpy` package. First, counts were normalized to 10 000 counts per cell, and then  $\log_{1p}$ -transformed. The transformed counts were projected to the top-50 principal components and 15-nearest neighbors were determined. Finally, clustering analysis was performed using the Leiden community detection algorithm with a resolution parameter of 1.

**Neighbor consistency** Neighbor consistency  $NC$  for the spot-neighbor graph was calculated according to

$$NC = \sum_{(v,w) \in E} \frac{\mathbb{1}_{c(v)=c(w)}}{|E|}, \quad (19)$$

where  $E$  denotes the set of neighboring vertex pairs and  $c(v)$  indicates the cluster assignment of vertex  $v$ .

**Effect of  $m$  (EMBRYO).** We sweep  $m \in \{0, 4, 8, 16, 32, 64, 128, 256\}$  on the in-house embryo dataset hvg gene set and report MAE, MSE, **PCC SPOT** (mean±std across spots), and **PCC GENE** (mean±std across genes); see Table S6. Overall,  $m$  has a clear impact: relative to the  $m=0$  baseline, errors decrease consistently as  $m$  increases. In particular, MSE improves from 0.255 to **0.202** (absolute change  $-0.053$ ,  $\sim 20.8\%$  reduction) and MAE from 0.270 to **0.234** (absolute change  $-0.036$ ,  $\sim 13.3\%$  reduction) at  $m=256$ . Correlations also benefit: the best **PCC SPOT** is reached at a moderate  $m=16$  (**0.572**  $\pm$  0.246, +0.015 over baseline), while **PCC GENE**

attains its highest values at both small and medium  $m$  ( $m=4$  and  $m=128$ :  $0.681 \pm \{0.171, 0.173\}$ , +0.018 over baseline).

Interestingly, small values of  $m$  already capture most of the gain. At  $m=4$ , we obtain MAE 0.237, MSE 0.207, **PCC SPOT**  $0.571 \pm 0.244$ , and **PCC GENE**  $0.681 \pm 0.171$ , recovering a large fraction of the improvement over  $m=0$ . For larger  $m \in [32, 256]$ , we observe diminishing returns: errors continue to decrease slightly (e.g., MSE 0.206  $\rightarrow$  0.202), while correlations remain effectively stable within  $\sim 0.002-0.005$ . Taken together, these results indicate that  $m$  controls a useful capacity/aggregation trade-off, but relatively small context sizes (e.g.,  $m=4-16$ ) already offer a strong balance between accuracy and efficiency.

**Effect of  $m$  (ST).** On the **ST** dataset (Table S7), increasing  $m$  yields clear accuracy gains up to a moderate context. Relative to  $m=0$  (MSE 0.443, MAE 0.532, **PCC SPOT**  $0.775 \pm 0.080$ , **PCC GENE**  $0.540 \pm 0.142$ ), performance improves steadily and peaks around  $m=32$ : MSE reaches **0.382** ( $-0.061$ ,  $\sim 13.8\%$  reduction), MAE **0.479** ( $-0.053$ ,  $\sim 10.0\%$  reduction), while correlations also increase to **0.786** (SPOT;  $+0.011$ ) and **0.572** (GENE;  $+0.032$ ). Notably, most of these gains are already realized by  $m=8-16$  (e.g., MSE 0.392, MAE 0.480 at  $m=16$ ), after which returns diminish and performance slightly plateaus ( $m \geq 32$ ).

**Effect of  $m$  (HER2).** For **HER2**, the effect of  $m$  is modest. Compared to  $m=0$  (MSE 0.477, MAE 0.534, **PCC SPOT**  $0.740 \pm 0.125$ , **PCC GENE**  $0.620 \pm 0.146$ ), the best results occur at  $m=16$ : MSE **0.462** ( $-0.015$ ,  $\sim 3.1\%$  reduction), MAE **0.530** ( $-0.004$ ,  $\sim 0.7\%$  reduction), **PCC SPOT** **0.741** ( $+0.001$ ) and **PCC GENE** **0.623** ( $+0.003$ ) Table S8. Beyond  $m \approx 16$ , curves remain essentially flat. We speculate this limited sensitivity arises from dataset and number of spot size: as summarized in Section S3, **HER2** contains relatively few spots, so enlarging  $m$  adds little additional neighborhood context. In regimes with sparse spatial neighborhoods, the proposed module may thus offer less scope for improvement, consistent with the small but nonzero gains observed here.

Table S6. Effect of  $m$  (powers of two) on performance for the **EM-BRYO** dataset. Lower is better for MAE/MSE; higher is better for PCC SPOT / PCC GENE. The  $m=0$  row is the provided baseline.

$m$	MSE ↓	MAE ↓	PCC SPOT (mean ± std) ↑	PCC GENE (mean ± std) ↑
0	0.255	0.270	$0.557 \pm 0.248$	$0.663 \pm 0.166$
4	0.207	0.237	$0.571 \pm 0.244$	<b><math>0.681 \pm 0.171</math></b>
8	0.212	0.241	$0.570 \pm 0.246$	$0.680 \pm 0.173$
16	0.210	0.240	<b><math>0.572 \pm 0.246</math></b>	$0.675 \pm 0.174$
32	0.206	0.236	$0.567 \pm 0.244$	$0.680 \pm 0.173$
64	0.204	0.236	$0.568 \pm 0.245$	$0.679 \pm 0.170$
128	0.203	0.235	$0.569 \pm 0.242$	<b><math>0.681 \pm 0.173</math></b>
256	<b>0.202</b>	<b>0.234</b>	$0.569 \pm 0.243$	$0.679 \pm 0.177$

Table S7. Effect of  $m$  on performance for the **ST** dataset. Lower is better for MAE/MSE; higher is better for PCC SPOT / PCC GENE.

$m$	MSE ↓	MAE ↓	PCC SPOT (mean ± std) ↑	PCC GENE (mean ± std) ↑
0	0.443	0.532	$0.775 \pm 0.080$	$0.540 \pm 0.142$
4	0.412	0.502	$0.781 \pm 0.014$	$0.561 \pm 0.101$
8	0.403	0.491	$0.782 \pm 0.012$	$0.563 \pm 0.098$
16	0.392	0.480	$0.784 \pm 0.012$	$0.571 \pm 0.012$
32	<b>0.382</b>	<b>0.479</b>	<b><math>0.786 \pm 0.012</math></b>	<b><math>0.572 \pm 0.038</math></b>
64	0.384	0.481	$0.780 \pm 0.045$	$0.569 \pm 0.019$

Table S8. Effect of  $m$  on performance for the **HER2** dataset. Lower is better for MAE/MSE; higher is better for PCC SPOT / PCC GENE.

$m$	MSE ↓	MAE ↓	PCC SPOT (mean ± std) ↑	PCC GENE (mean ± std) ↑
0	0.477	0.534	$0.740 \pm 0.125$	$0.620 \pm 0.146$
4	0.473	0.533	$0.739 \pm 0.010$	$0.618 \pm 0.013$
8	0.471	0.533	$0.740 \pm 0.011$	$0.62 \pm 0.037$
16	<b>0.462</b>	<b>0.530</b>	<b><math>0.741 \pm 0.023</math></b>	<b><math>0.623 \pm 0.012</math></b>
32	0.472	0.533	$0.740 \pm 0.021$	$0.621 \pm 0.023$

Table S9. Average number of spots per dataset.

HER2	ST	EMBRYO
378	482	6353

Table S10. Spot-level performance on the even-slice hold-out split for different ablation settings on the in-house embryo dataset. For each panel size, the best value is shown in **bold**. Lower is better for MSE/MAE; higher is better for PCC.

Regime	Genes	MSE ↓	MAE ↓	PCC(GENE) ↑
Vanilla STFlow	50	0.160	0.107	0.693
	100	0.177	0.120	0.688
	200	0.176	0.119	0.673
	500	0.164	<b>0.124</b>	0.646
Vanilla + Learned Prior	50	0.181	0.127	0.691
	100	0.175	0.116	0.690
	200	0.161	0.114	0.680
	500	0.164	0.134	0.642
ControlNet + Learned Prior	50	<b>0.154</b>	0.096	<b>0.701</b>
	100	0.169	0.117	0.692
	200	0.155	0.108	0.694
	500	0.164	0.127	0.651
ControlNet + Learned Prior + Cross Slide Neighbors	50	0.155	<b>0.092</b>	0.695
	100	<b>0.158</b>	<b>0.112</b>	<b>0.697</b>
	200	<b>0.147</b>	<b>0.108</b>	<b>0.698</b>
	500	<b>0.162</b>	0.128	<b>0.654</b>

Section	GT	Imp
22	0.804	0.851
31	0.738	0.851
40	0.752	0.906
47	0.709	0.856
50	0.769	0.872
54	0.675	0.846
64	0.664	0.846
70	0.774	0.860
76	0.768	0.853
84	0.787	0.856
91	0.803	0.842
101	0.804	0.840
111	0.771	0.843
124	0.751	0.841
131	0.748	0.848
137	0.757	0.856
142	0.777	0.868
151	0.513	0.868
161	0.517	0.891
172	0.822	0.918
182	0.826	0.909
192	0.887	0.915
205	0.850	0.928
221	0.954	0.975
241	0.961	0.994
252	0.976	0.966
mean	0.775	0.881
std	0.109	0.045

Figure S1. Neighbor consistency of joint clustering across 26 unseen sections. GT: ground truth, Imp: imputed, std: standard deviation.

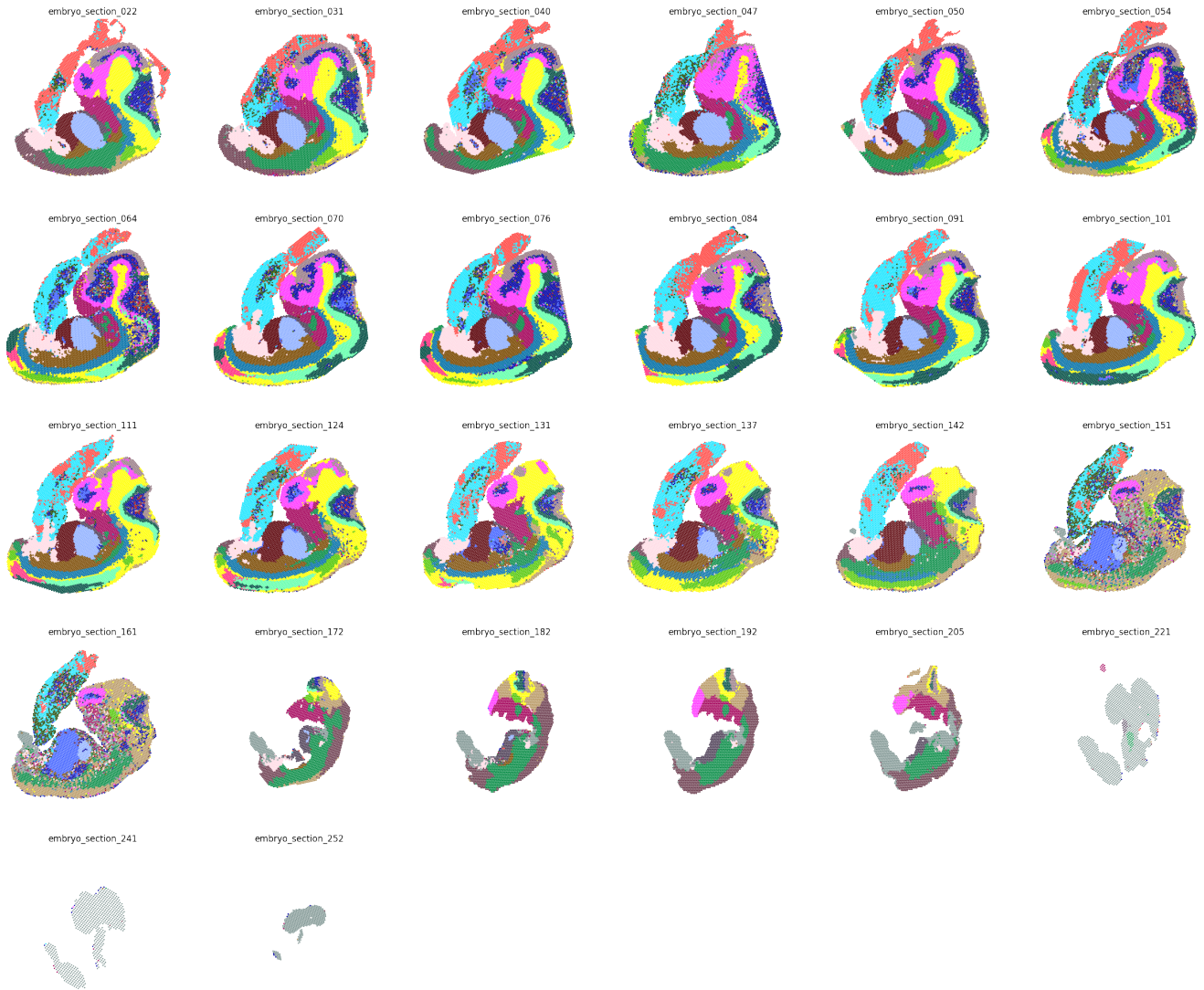


Figure S2. Joint clustering of the ground truth expression across all 26 sections not seen during training.

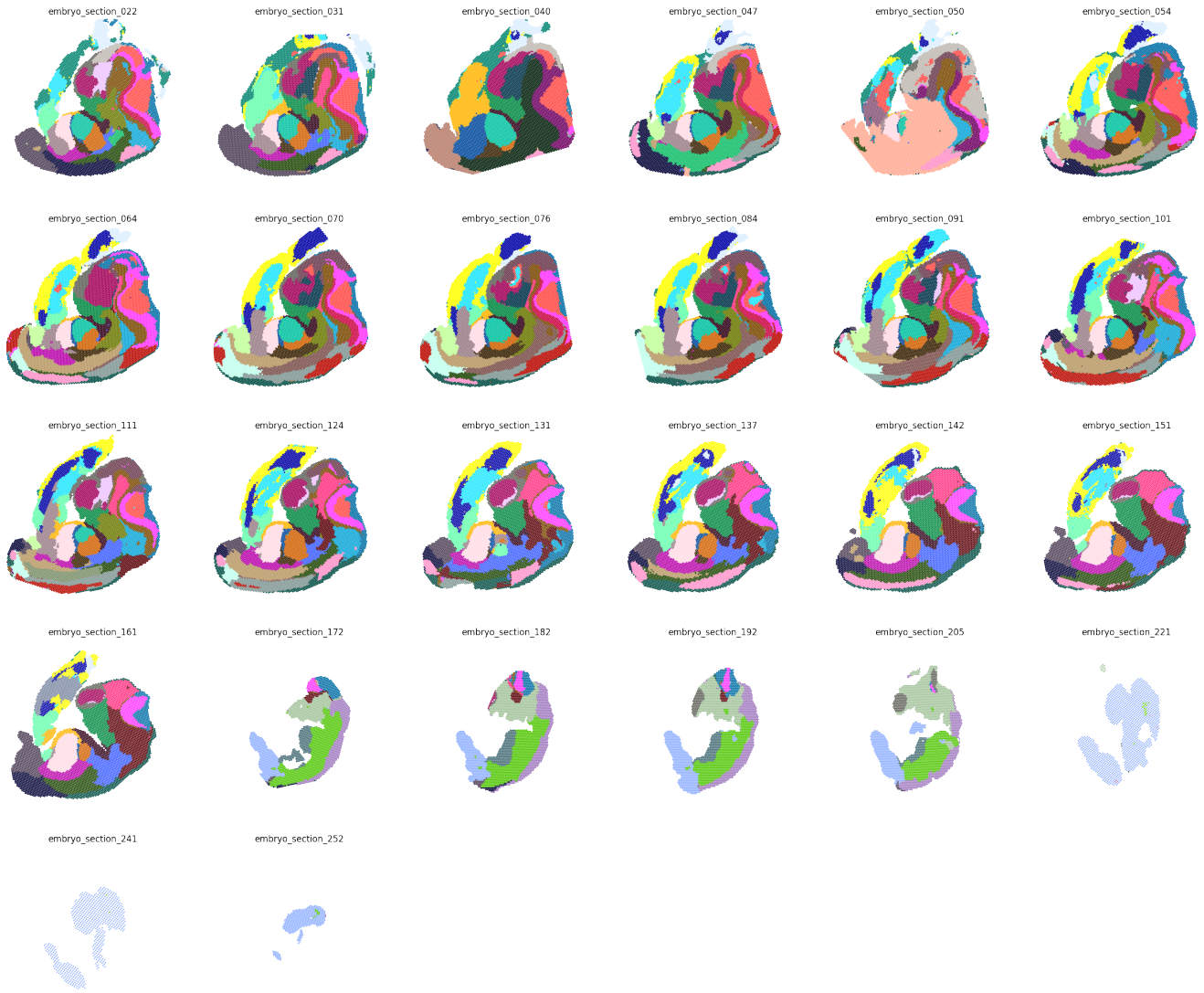


Figure S3. Joint clustering of the imputed expression across all 26 sections not seen during training.

